PAPER

Effect of Er/Y addition on the growth and superconductivity of Bi2212 films

Bowen Zhang[a] and Yang Qi ⓘ *[ab]

In order to increase the critical current density of Bi2212 superconducting films to broaden their application areas. A series of $Bi_2Sr_2CaCu_2O_{8+\delta}-xRE_2O_3$ (RE = Er/Y) (x = 0, 0.04, 0.08, 0.12, 0.16, 0.20) thin films were prepared by the sol−gel method. The structure, morphology and superconductivity of the RE_2O_3 doping films were characterized in detail. The effect of RE_2O_3 on the superconductivity of Bi2212 superconducting films was investigated. It was shown that the Bi2212 films were (00l) epitaxially grown. The in-plane orientation relationship between the $Bi2212-xRE_2O_3$ and the $SrTiO_3$ was Bi2212[100](001)// $SrTiO_3$[011](100). The grain size in the out-of-plane direction of Bi2212 tends to increase with the amount of RE_2O_3 doping. Doping with RE_2O_3 had no significant effect on the anisotropy of Bi2212 crystal growth, but inhibited the agglomerative growth of the precipitated phase on the surface to a certain extent. Furthermore, the conclusion was that the superconducting transition temperature ($T_{c,onset}$) was almost unaffected, while the zero resistance transition temperature ($T_{c,zero}$) continued to decrease with increasing doping level. The thin film samples Er2 (x = 0.04) and Y3 (x = 0.08) exhibited the best current-carrying capacity in magnetic fields.

Introduction

Since the discovery of bismuth-based high-temperature superconducting materials (HTSC), researchers have attempted to modify their structures through various techniques to improve the magnetic and superconducting properties of superconducting materials.[1–4] Bi2212 has been widely studied for its small power loss, high current, magnetic field carrying capacity, electronic properties, and structural properties. However, the application of Bi-based superconductors has significant limitations in terms of critical current density, such as weak integration and weak flux pinning.[5] The replacement of elements in Bi-based superconductors and the addition of second-phase substances have been shown to be an effective means of improving their superconductivity and magnetic properties. These works have been extensively investigated.[6–9] In this case, the trend of the superconducting properties is closely related to the properties of the dopant in the crystal structure.[5] The phase structure and physical properties of Bi2212 superconductors can be modified by replacing or adding elements with different ionic radii or different binding properties.

Rare earth elements exhibit special physical and chemical properties in the fields of optics, electricity and magnetism due to their unique electronic structure. Rare earth metals and their

compounds have good applications. Rare earth elements play an important role in almost all high-temperature superconducting materials. For example, the addition of Sm_2O_3 nanoparticles improved electrical transport properties of Bi2223 at very low doping levels.[10] The addition of small amounts of Nb improved the Bi2223 grain boundary connectivity, resulting in better superconductivity of the BSCCO system.[11] In addition, the substitution of rare earth ions is an effective means to improve the superconducting transition temperature and critical current density by adjusting the phase structure and microstructure.[12–15] Besides, rare earth elements are also widely used in the REBCO family. Substitution of Y by RE elements can improve their superconductivity properties in different ways, such as lower processing temperature and wider processing window for smaller RE ions[16,17] and higher critical transition temperature for larger RE ions.[18,19]

The main factors that reduce the critical current density of HTSC are grain boundaries and poor flux pinning.[20] Low values of critical current density at grain boundaries in polycrystalline samples are an important issue for high current applications, for which increasing the critical current density is a key issue. The nanoscale superconductivity has attracted much attention during the past decades.[21–23] The presence of flux pinning centers in non-ideal class II superconductors due to crystal structure defects will greatly increase their current-carrying capacity in both self-magnetic fields and external magnetic fields, making high-temperature superconductors extremely promising for applications in the strong direction. The property led scientists to search for forms of high-temperature

[a]Department of Materials Physics and Chemistry, School of Materials Science and Engineering, State Key Laboratory of Rolling and Automation, Northeastern University, Shenyang, Liaoning 110819, PR China. E-mail: qiyang@imp.neu.edu.cn
[b]Key Laboratory for Anisotropy and Texture of Materials, Ministry of Education, Northeastern University, Shenyang, 110819, P. R. China

superconductors with stronger current-carrying capacity by artificially designing the shape, density and distribution of pinning centers.[24–27] Related studies have shown that the nanoscale second phase has superior properties J_c values as a pinning center for superconductors. In contrast, the effect of doping of Er and Y elements on Bi2212 has rarely been investigated.

We have conducted extensive studies on the preparation of Bi2212 superconducting films by sol–gel method with aqueous solvents.[28–31] It was shown that this environmentally friendly and low-cost method can prepare high quality Bi2212 superconducting films. At the same time, the sol–gel method can maintain homogeneity at the atomic level. Therefore, the method offers irreplaceable advantages for the preparation of highly dispersive doped Bi2212 samples as well.

In this chapter, Bi2212 superconducting films with different RE (RE = Er/Y) doping amounts were prepared on SrTiO$_3$(100) substrates using the sol–gel method. To investigate the optimal conditions for RE$_2$O$_3$ doping of Bi2212 superconducting films. And to explore its effects on the crystallographic properties, surface morphology and electrical transport properties of Bi2212 superconducting films.

Experimental

In this chapter, Bi$_2$Sr$_2$CaCu$_2$O$_{8+\delta}$–xRE$_2$O$_3$ (Bi2212–xRE$_2$O$_3$) (RE = Er/Y) (x = 0, 0.02, 0.04, 0.06, 0.08, 0.10) superconducting films were prepared by the sol–gel method. The analytical reagents Bi(NO$_3$)$_3$–5H$_2$O, Sr(NO$_3$)$_2$, Ca(NO$_3$)$_2$–4H$_2$O, Cu(NO$_3$)$_2$–3H$_2$O, Er(NO$_3$)$_3$–6H$_2$O and Y(NO$_3$)$_3$–6H$_2$O were used as reactants in the molar ratio Bi : Sr : Ca : Cu = 2 : 2 : 1 : 2. Glycine was used as complexing agent and deionized water was used as solvent. The blue colored sol was obtained after stirring. 2 mL of nitric acid was added to the Bi2212 sol to maintain an acidic environment and made the sol more stable. 5 wt% PVP solution was added to give a concentration of c(PVP) = 0.5 wt%. The 0.5 wt% PVP in the sol was more favorable for the sol to form a thin film by the spin coating method.

After coating the sol–gel films on the SrTiO$_3$(100) substrate, the precursor films were heated at 413 K for 40 min to form the precursor films. To obtain a certain thickness of sample, this process was repeated three times. The samples were then heat treated in the tube furnace with a sintering temperature of 1098 K and a holding time of 35 min to form the final Bi2212 films. The Bi2212–xEr$_2$O$_3$ samples were named as the Er group, named Er1–Er6 in that order. The Bi2212–xY$_2$O$_3$ samples were named as the Bi2212–xY$_2$O$_3$ samples were named as Y group and named as Y1–Y6 in order. All the samples were sintered at 1098 K with a holding time of 35 min.

The phase composition and crystallinity of the superconducting films were characterized by a Rigaku-Smart Lab X-ray diffractometer (Cu-Kα radiation). The θ–2θ scan range was 3°–50°, with a scan step of 0.02° and a scan speed of 1° min^{-1}. The Phy scan and swing curves of the films were characterized by a Smartlab(3) X-ray diffractometer (Cu-Kα radiation). The surface morphology of the Bi2212 superconducting films was observed by field emission scanning electron microscopy (FESEM) (Zeiss). The surface structure was further investigated by atomic force microscopy (AFM) (Nanoscan Easy2) and the surface roughness of the samples was counted, using a non-contact tap mode. X-ray photoelectron spectroscopy (XPS) was obtained using a Kratos-Axis Supra from Shimadzu Corporation, Japan. X-ray photoelectron spectrometer. The superconducting properties of the samples were measured by the standard four-probe method. The Physical Property Measurement System (PPMS) measures in the temperature range of 2–300 K and in the magnetic fields range of 0–9 T.

Results and discussion

The crystallographic properties of the samples were characterized by XRD. As shown in Fig. 1, Fig. 1(a) showed the XRD pattern of the Er1–Er6 samples and Fig. 1(b) showed the XRD pattern of the Y1–Y6 samples. The detailed crystallographic information was shown in Table 1. As can be seen in Fig. 1(a) and (b), only the diffraction peak of Bi2212(00l) can be observed in all samples, indicating that the prepared thin film samples were all grown in c-axis selective orientation. The diffraction peaks near 5.750°, 17.308°, 23.147°, 29.048° and 35.028° correspond to the (002), (006), (008), (0010) and (0012) crystal planes of Bi2212 (PDF 79-2183), respectively. The rest of the diffraction peaks in Fig. 1(a) were all SrTiO$_3$ diffraction peaks
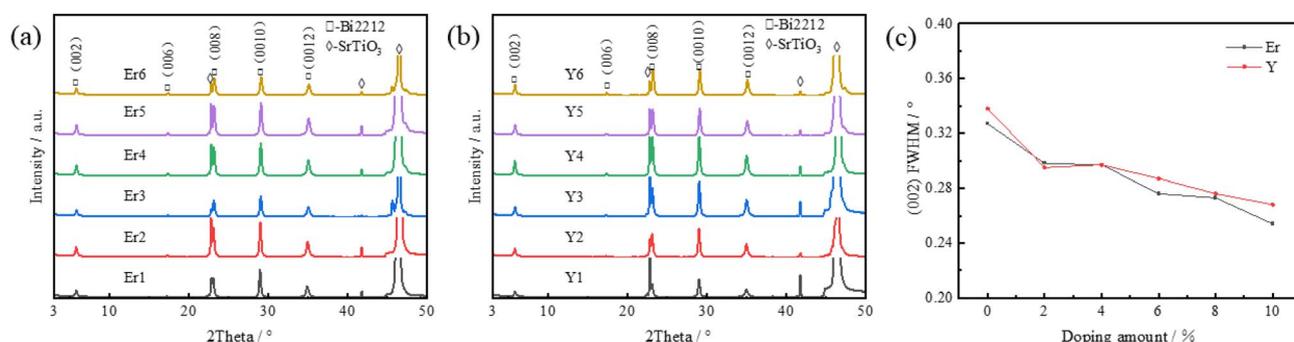

Fig. 1 XRD patterns of the samples. (a) XRD patterns of samples Er1–Er6. (b) XRD patterns of samples Y1–Y6. (c) FWHM variation of RE-doped Bi2212 superconducting films.

Table 1 Crystallographic properties of samples

| Sample	Doping amount/%	(002) peak position/°	X_{Bi2212}/%	(002) FWHM/°	Grain size/nm	Rms/nm
Er1	0.00	5.79	97.1	0.33	26.2	12.2
Er2	0.04	5.77	98.3	0.30	29.6	11.9
Er3	0.08	5.81	95.8	0.30	28.2	17.3
Er4	0.12	5.81	95.8	0.28	29.2	11.4
Er5	0.16	5.81	95.7	0.27	31.1	11.0
Er6	0.20	5.81	95.9	0.25	31.5	10.9
Y1	0.00	5.79	97.2	0.34	24.9	9.6
Y2	0.04	5.79	97.2	0.30	28.4	11.1
Y3	0.08	5.79	96.9	0.30	27.6	12.1
Y4	0.12	5.79	97.0	0.29	30.5	14.7
Y5	0.16	5.81	95.8	0.28	32.9	15.3
Y6	0.20	5.81	95.7	0.27	33.5	13.1
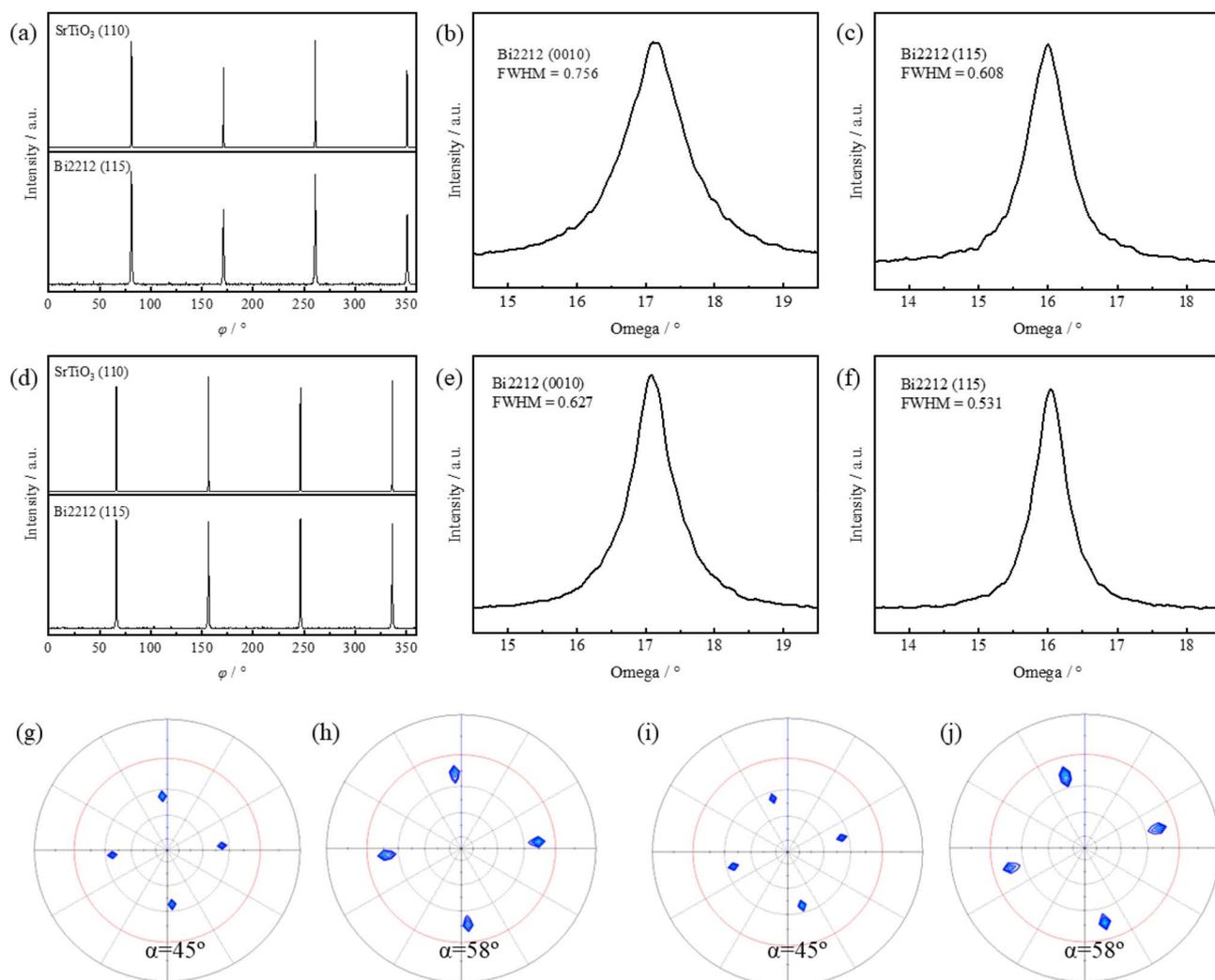
Fig. 2 (a) Phy scan XRD scans of the Bi2212(115) and SrTiO₃(110) surfaces of sample Er6. (b) ω scan XRD pattern of the Bi2212(0010) of sample Er6. (c) ω scan XRD pattern of the Bi2212(115) of sample Er6. (d) Phy scan XRD scans of the Bi2212(115) and SrTiO₃(110) surfaces of sample Y6. (e) ω scan XRD pattern of the Bi2212(0010) of sample Y6. (f) ω scan XRD pattern of the Bi2212(115) of sample Y6. (e) ω scan XRD pattern of the Bi2212(0010) of sample Y6. (f) ω scan XRD pattern of the Bi2212(115) of sample Y6. (g) X-rays pole figures for SrTiO₃(110) plane of Er-6. (h) X-rays pole figures for Bi2212(115) plane of Er6. (i) X-rays pole figures for SrTiO₃(110) plane of Y-6. (j) X-rays pole figures for Bi2212(115) plane of Y6.

and the rest of the diffraction peaks in Fig. 1(b) were also SrTiO$_3$ diffraction peaks. We found that the diffraction peak of Bi2212 was shifted towards a high angle. This was due to the presence of the intergrowth phase (Bi2212$_x$Bi2201$_{1-x}$) in Bi2212. Therefore, we need to calculate the purity of Bi2212 in the samples as in eqn (1).[32,33]

$$X_{\mathrm{Bi2212}} = (\theta_{\mathrm{Bi2201}} - \theta)/(\theta_{\mathrm{Bi2212}} - \theta_{\mathrm{Bi2201}}) \tag{1}$$

where θ, θ_{Bi2201} and θ_{Bi2212} are the diffraction peak position of intergrowth phase, the pure Bi2201 phase (002) crystal plane (PDF 79-2181) and the pure Bi2212 phase (002) crystal plane, respectively. The calculated results were shown in Table 1. The purity of the Bi2212 phase in the films were all above 95%. The crystallinity of the samples was good and their grain size was calculated by the Scherrer formula,[34] the results were shown in Table 1. The RE$_2$O$_3$ diffraction peaks could not be observed in the XRD pattern due to the low doping amount. This may be due to poor crystallinity and less content.

In order to further analyze the crystallinity of the samples, the half-height widths (FWHM) and grain sizes were counted and the information was shown in Table 1. The grain sizes were calculated from the Scherrer formula. The results showed that the Bi2212 sample had good crystallinity and there was an increasing trend of grain size with increasing RE$_2$O$_3$ doping in the out-of-plane direction of the sample, as shown in Fig. 1(c).

This may be due to the addition of the second phase reducing the microstrain in the film matrix. It resulted an increase in the grain size of the film.[35,36] In summary, Bi2212–xRE$_2$O$_3$ (RE = Er/Y) superconducting films with high phase purity and good crystalline quality were fabricated on SrTiO$_3$(100) substrates.

XRD-φ scans was used to analyze the in-plane orientation relationships of samples Er6 and Y6. XRD patterns were shown in Fig. 2. The φ-scan of the Bi2212(115) and SrTiO$_3$(110) of sample Er6 were shown in Fig. 2(a), and the φ-scan XRD patterns of the Bi2212(115) and SrTiO$_3$(110) of sample Y6 were shown in Fig. 2(d). As can be seen from the figures, both Er6 and Y6 exhibited good quadratic symmetry. φ diffraction peaks on the (115) face of Er6 were 80.9°, 170.9°, 260.9° and 350.9°, which were consistent with those on the SrTiO$_3$(110) face. φ diffraction peaks on the (115) face of Y6 were 66.1°, 156.1°, 246.1° and 336.1°, which were consistent with the φ diffraction peak positions of the SrTiO$_3$(110) crystal plane. The pole figures were shown in Fig. 2(g)–(j). It can be clearly found that Bi2212 had quartic symmetry. The crystal plane (115) had four clear diffraction poles at $\alpha = 58°$, and no other poles, indicating that the plane had only one growth orientation. The SrTiO$_3$ single crystal substrate (110) plane also had four clear diffraction poles only at $\alpha = 45°$. This shows that the Bi2212 phase also exhibited quartic symmetry and had only one orientation. On this basis, the in-plane epitaxial matching relation of thin films was further proved by the calculation of crystal band theorem.
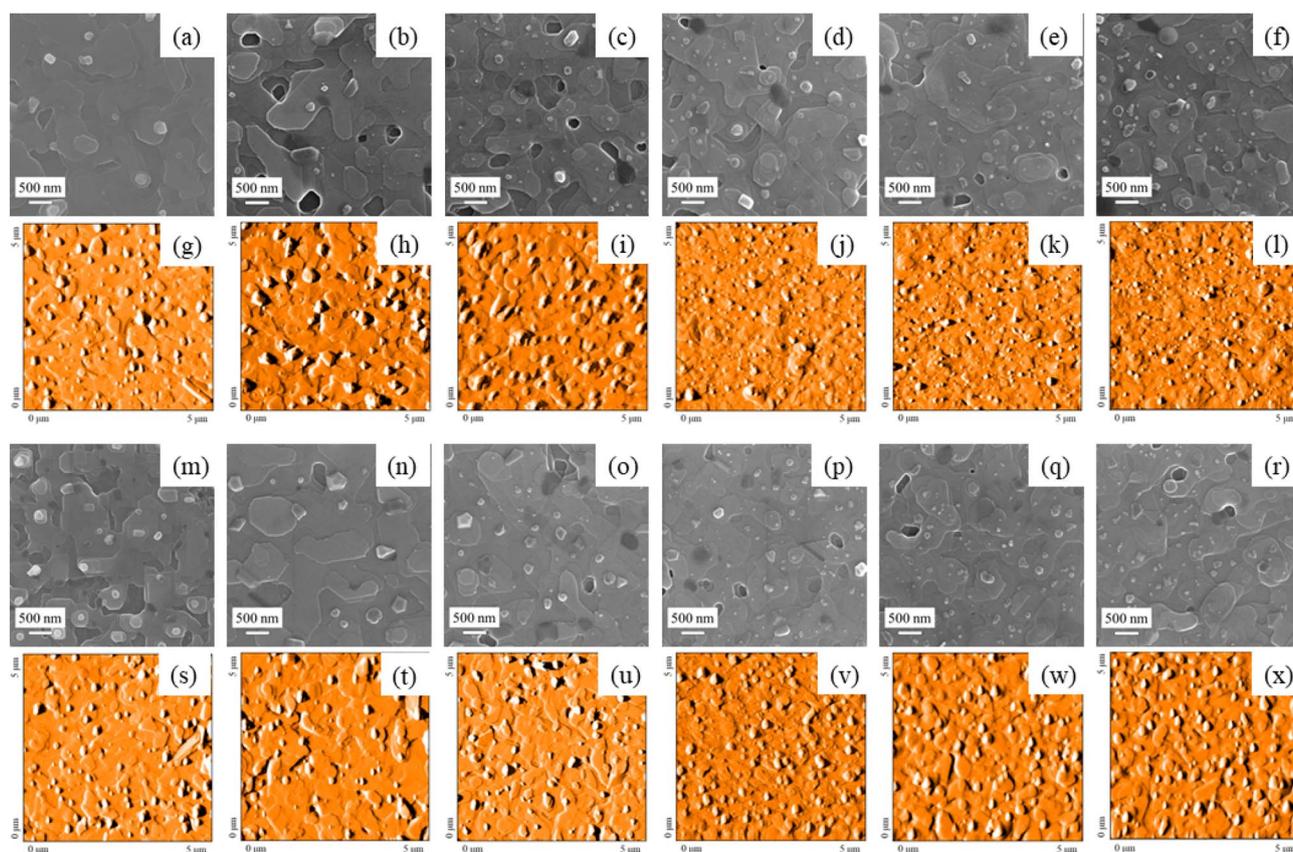

Fig. 3 SEM images and AFM images of Bi2212 superconducting films. (a)–(c) and (g)–(i) were SEM images of Er1–Er6, respectively. (d)–(f) and (j)–(l) were AFM images of Er1–Er6, respectively. (m)–(r) were SEM images of Y1–Y6, respectively. (s)–(x) were AFM images of Y1–Y6, respectively.

According to the crystal band theorem, the index [uvw] of the axial axis T of the crystal band can be expressed as (2)

$$u : v : w = \frac{h_1}{h_2}\begin{vmatrix}k_1\\k_2\end{vmatrix} \times \frac{l_1}{l_2} \times \frac{h_1}{h_2} \times \begin{vmatrix}k_1\\k_2\end{vmatrix} \frac{l_1}{l_2} = (k_1 l_2 - k_2 l_1) : (l_1 h_2 - l_2 h_1) : (h_1 k_2 - h_2 k_1)$$

(2)

It was calculated that [$1\bar{1}0$] was the crystal band axis of Bi2212(00l) crystal plane with the (115) crystal plane. Similarly, it followed that [$00\bar{1}$] was the crystal band axis between the SrTiO$_3$(100) crystal plane and the (110) crystal plane. Therefore, the in-plane matching relation between the Bi2212 substrate and the SrTiO$_3$(100) substrate was Bi2212[100](001) ∥ STO [011](100). Meanwhile, Fig. 2(b) and (c) showed the ω-scan XRD patterns of Bi2212(0010) and (115) for the Er6 sample, and Fig. 2(e) and (f) showed the ω-scan XRD patterns of Bi2212(0010) and (115) for the Y6 sample, and it can be found that the in-plane and out-plane crystallinity of the Bi2212 superconducting films were good. The results showed that RE$_2$O$_3$ doping did not change the (00l) epitaxial growth characteristics of all the Bi2212 superconducting films on SrTiO$_3$(100) single crystal substrates, and the films had good crystallinity.

The surface morphology of samples Er1–Er6 was characterized by FESEM and AFM, as shown in Fig. 3. Fig. 3(a)–(c) and (g)–(i) showed the SEM images of Er1–Er6, respectively. Fig. 3(d)–(f) and (j)–(l) showed the AFM images of Er1–Er6, respectively. It can be observed that the surfaces of all samples were continuous and smooth. In addition to this, the surface of the film showed mainly a lamellar structure. This was mainly due to the anisotropy of the Bi2212 growth rate. The fast in-surface growth rate resulted in a two-dimensional characteristic shape of the sample.[37] The surface morphology and structure of the samples Er1–Er6 was further characterized by

AFM, and as can be seen in Fig. 3(d)–(f) and (j)–(l), the lamellar morphology of the films was characterized, in agreement with the FESEM images. The surface roughness of Er1–Er6 was 12.2 nm, 11.9 nm, 17.3 nm, 11.4 nm and 11.0 nm. The roughness statistics were shown in Table 1. The doping of Er$_2$O$_3$ did not significantly change the surface roughness. The addition of Er$_2$O$_3$ inhibited the enrichment and growth of the precipitated phase particles, resulting in a uniform and diffuse distribution of the precipitated phase particles. The surface morphology of samples Y1–Y6 was also characterized by FESEM and AFM, as shown in Fig. 3. Fig. 3(m)–(r) showed the SEM images of Y1–Y6, and Fig. 3(s)–(x) showed the AFM images of Y1–Y6, respectively. It can be found that the surfaces of the Y1–Y6 samples continued to show a continuous and smooth lamellar morphology. The surface roughness of Y1–Y6 was 9.6 nm, 11.1 nm, 12.1 nm, 14.7 nm, 15.3 nm and 13.1 nm, respectively. The specific roughness was shown in Table 1.

The elemental distributions of the Er6 and Y6 samples were characterized by EDS spectroscopy, respectively. The results were shown in Fig. 4. Fig. 4(a) showed the surface morphology of the Er6 sample and its distribution of Bi, Ca, Cu, and Er elements, while Fig. 4(b) showed the surface morphology of the Y6 sample and its distribution of Bi, Ca, Cu, and Y elements. The distribution of Sr elements was not characterized because the SrTiO$_3$ single crystal substrate contained Sr elements. From the figure, it can be observed that the three elements Bi, Ca and Cu were uniformly distributed without component segregation in the Er6 and Y6. Similarly, no segregation was observed for Er and Y, demonstrating that Er and Y were uniformly and diffusely distributed in the film matrix.

The XPS spectra of samples Er6 and Y6 were shown in Fig. 5 to further confirm the presence of the doping elements in Bi2212 and their chemical valence. Both spectra in Fig. 5(a) and (c) confirmed the presence of bismuth, strontium, calcium, copper, oxygen and carbon in both samples, with a binding
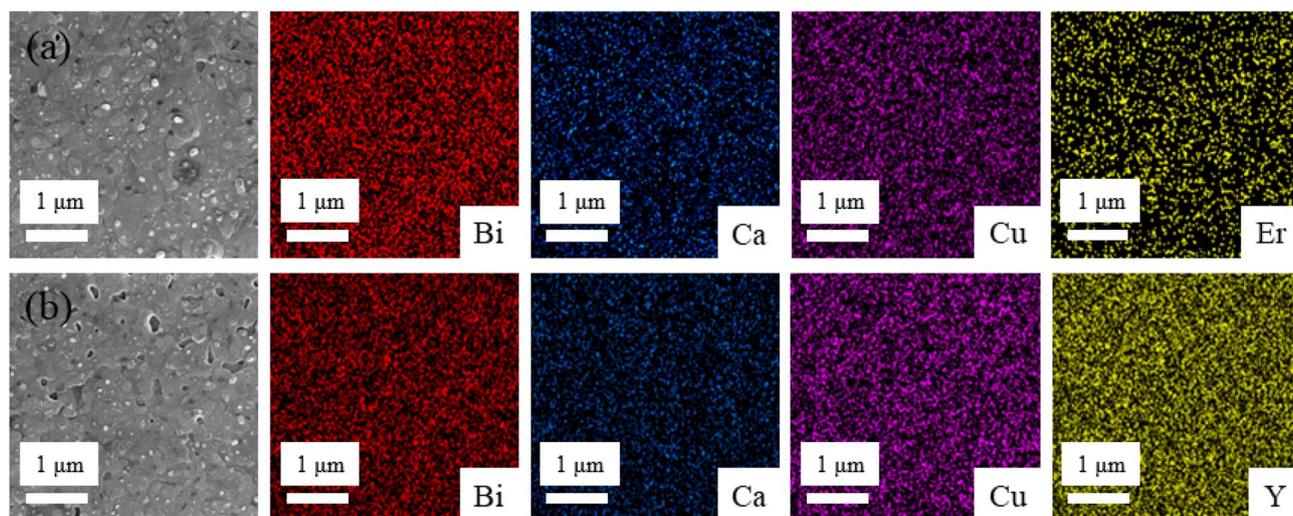

Fig. 4 Surface morphology of Bi2212 superconducting films. (a) SEM image of Er6 sample, Bi elemental distribution, Ca elemental distribution, Cu elemental distribution and Er elemental distribution. (b) SEM image of Y6 sample, Bi element distribution, Ca element distribution, Cu element distribution and Y element distribution.
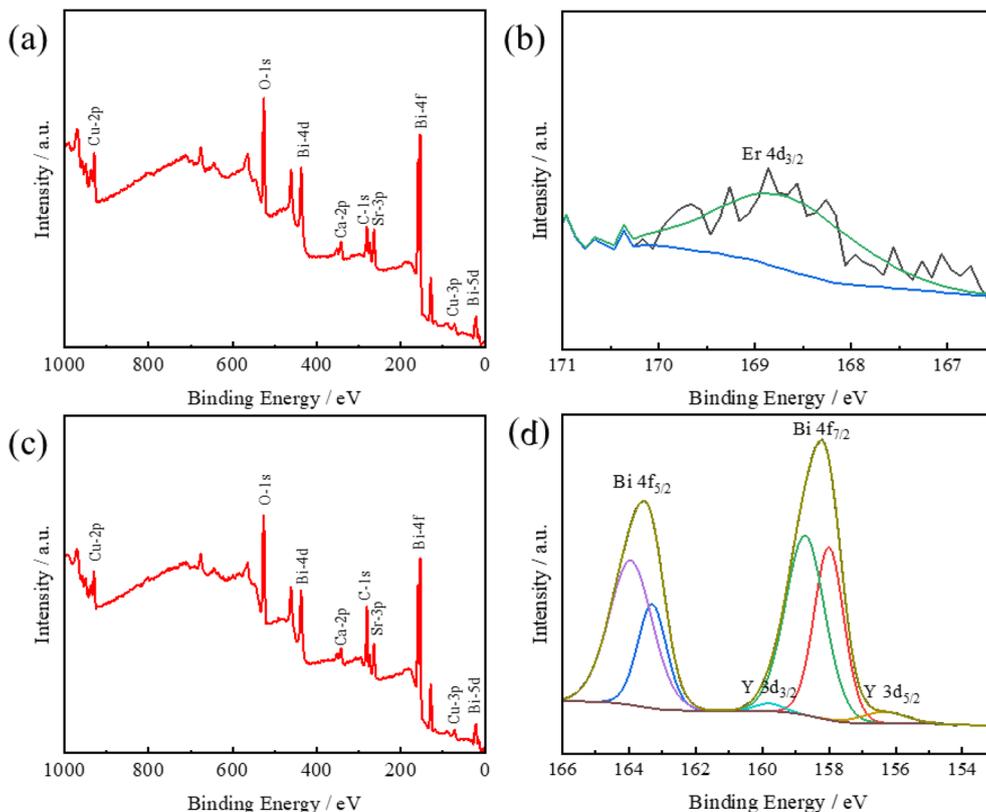
Fig. 5 XPS spectra of (a) survey scan of Er6; (b) Er region of Er6; (c) survey scan of Y6; (d) Y region of Y6.
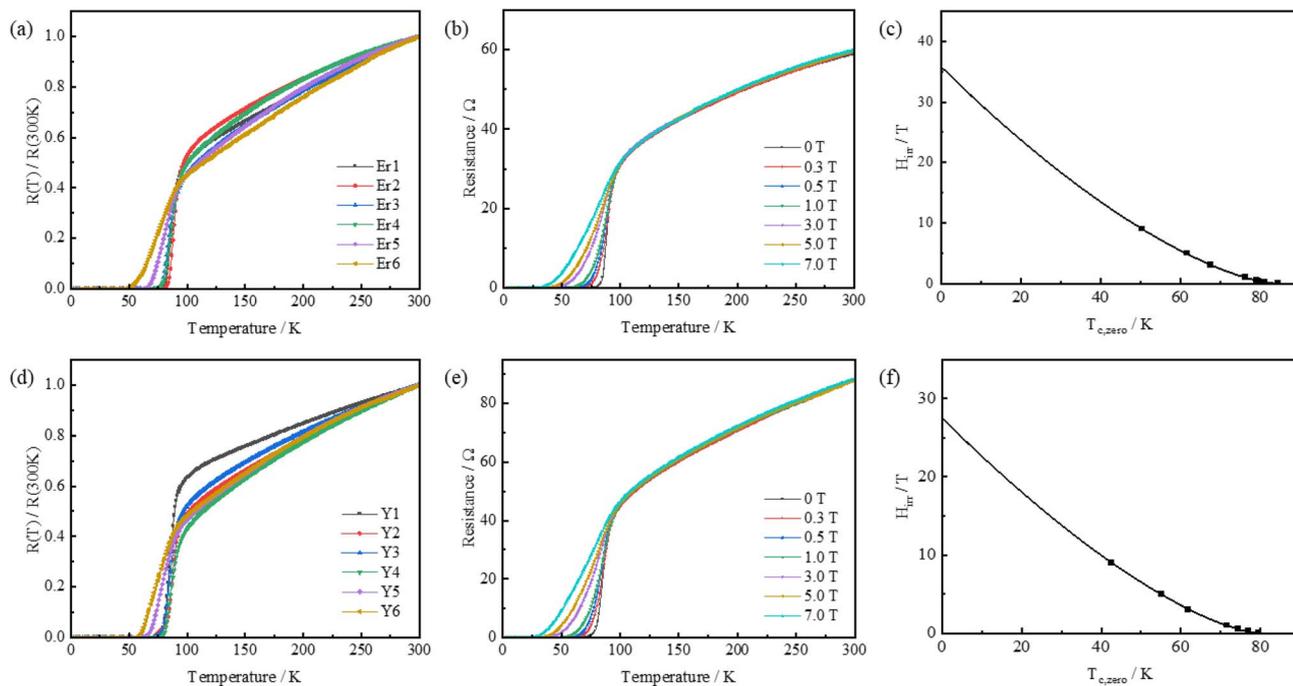

Fig. 6 (a) Electrical transport properties of samples Er group. (b) Temperature dependence of the resistances of Er2 in magnetic fields from 0 T to 9 T. (c) Temperature dependence of the irreversible field H_{irr} of sample Er2. (d) Electrical transport properties of samples Y group. (e) Temperature dependence of the resistances of Y3 in magnetic fields from 0 T to 9 T. (f) Temperature dependence of the irreversible field H_{irr} of sample Y3.

energy of 284.8 eV for C 1s, which was typical for C–C compounds and used for reference correction. The fit of Er 4d showed a peak at 168 eV as shown in Fig. 5(b), which was consistent with previously reported data.[38] In Fig. 5(d), the Y 3d spectrum was decomposed into two peaks at 160.5 eV and 158.3 eV, corresponding to the high bound state of Y $3d_{3/2}$ and the low bound state of Y $3d_{5/2}$, respectively. These two peaks were typical of Y_2O_3 and indicate the presence of the Y^{3+} oxidation state in the sample.[39]

The electrical transport properties of the Bi2212 superconducting films were shown in Fig. 6, where Fig. 6(a) showed the electrical transport properties of the sample Er group of

Table 2 Electrical transport properties of samples

Sample	$T_{c,onset}$/K	$T_{c,zero}$/K	ΔT_c/K
Er1	92.7	81.9	10.8
Er2	92.7	81.4	11.3
Er3	92.1	79.1	13.0
Er4	92.0	77.8	14.2
Er5	93.2	69.3	23.9
Er6	91.8	57.2	34.6
Y1	90.9	80.1	10.8
Y2	92.8	81.4	11.4
Y3	92.5	80.7	11.8
Y4	93.6	80.8	12.8
Y5	90.8	68.4	22.4
Y6	90.3	60.0	30.3

samples. Fig. 6(b) showed the temperature dependence of the resistance of the Er2 sample in a magnetic field from 0 T to 9 T. Fig. 6(c) showed the temperature dependence of the irreversibility field of $H_{irr} \propto (1 - T/T_c)^{\beta}$[40–42] (black line) fitted to Er2, with the specific information shown in Table 2. As seen in Fig. 6(a), the sample exhibited good metallic state resistance behavior characteristics in the temperature range of 300–120 K under a magnetic field of 0 T. The temperature–resistance curve was linearly dependent. As the temperature continued to decrease, the R–T curve began to deviate from the linear relationship and the resistance value decreased sharply, at which point it was the superconducting transition process. As the temperature continued to decrease, the resistance value of the film dropped to zero, at which point the sample completed. The $T_{c,onset}$ values of Er1–Er6 were 92.7 K, 92.7 K, 92.1 K, 92.0 K, 93.2 K and 91.8 K. The $T_{c,onset}$ values only decreased slightly at higher doping levels. This highly diffusely distributed second phase benefited from the intrinsic advantages of the sol–gel method. The atomic-level homogeneity ensured during the preparation process then greatly avoided the production of hard agglomerates of Bi2212 precursors while suppressing the agglomerative growth of the second phase material. This was a prerequisite for our preparation of Bi2212–xRE$_2$O$_3$ (RE = Er/Y) with good superconductivity. The $T_{c,zero}$ values were 81.9 K, 81.4 K, 79.1 K, 77.8 K, 69.3 K and 57.2 K. It can be seen that the $T_{c,zero}$ values decreased monotonically with increasing doping levels. The presence of second phase material in the film. This increased the thickness of the insulating grain boundaries in the film
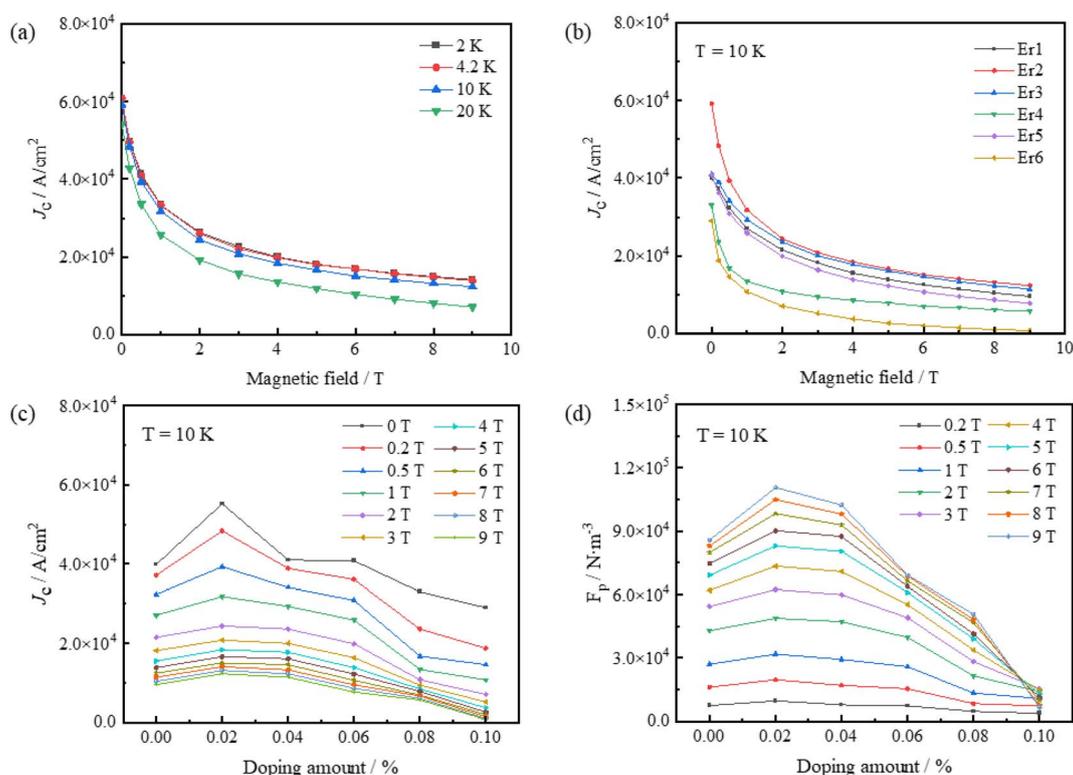

Fig. 7 (a) J_c of sample Er2 at different magnetic fields; (b) variation of J_c with magnetic field for Er group samples at 10 K; (c) variation of J_c with doping level for Er group samples at 10 K; (d) F_p versus doping level at different magnetic fields for Er group samples at 10 K.

matrix. Then, it led to an increase in the intergranular coupling energy required for the superconducting current to pass through the penetration. Thus, more grain boundary regions were required for the superconducting current to flow through to complete the superconducting transition.

Increasing the magnetic field from 0 T to 9 T, the R–T curves of the Er2 sample in the magnetic field from 0 T to 9 T were shown in Fig. 6(b), the sample still showed good metallic state resistance behavior characteristics in the temperature range of 300–120 K; when the temperature continued to decrease, the R–T curve started to deviate from the linear relationship, the resistance value decreased sharply and the superconducting transition process began. As the magnetic field increased, $T_{c,zero}$ obviously moved in the direction of low temperature, and the value of ΔT_c gradually increased. This was due to the fact that when the external magnetic field $H_{c1} < H < H_{c2}$, the magnetic lines of force formed a normal state core in the form of a two-dimensional pie-shaped flux vortex in the high-temperature superconductor, surrounded by a superconducting current externally. As the external magnetic field increased, resulting in an increasing normal-state core region, a decreasing super-conducting fraction, a decreasing $T_{c,zero}$ with increasing magnetic field and an increasing ΔT_c value.[43] The irreversibility field (H_{irr}) of the Er2 sample was fitted by eqn (3) and the results were shown in Fig. 6(c).

$$H_{irr} \propto (1 - T/T_c)^\beta \qquad (3)$$

where T was the critical temperature value under the external magnetic field and T_c was the critical temperature value under the self-field. Where the fitted irreversible lines indicated that sample Er2 was expected to have an irreversible magnetic field of more than 30 T at 0 K. This strong irreversible magnetic field indicated that the Bi2212 superconducting film prepared by the sol–gel method had some potential applications. The R–T characteristics of the group Y samples were shown in Fig. 6(d)–(f). It can be noticed that the R–T properties of the group Y samples showed the same pattern, indicating that the group Y samples were Bi2212–xY₂O₃ samples with Y₂O₃ in the form of a second phase.

The effect of Er₂O₃ on the critical current density (J_c) of Bi2212 superconducting films was shown in Fig. 7. The external magnetic field was tested perpendicular to the surface of Bi2212 superconducting films ($M \perp ab$-plane) with a maximum magnetic field of 9 T. The variation of J_c with doping level for the samples in the Er group at 10 K was shown in Fig. 7(c). It can be seen from the figures that J_c decreased with increasing magnetic field for all samples. The decay rate decreased gradually, which was due to the joint result of the intrinsic pinning of the thin film samples and the Er₂O₃ pinning, which was stronger at higher magnetic fields, in agreement with the above results. In addition, it can be seen that sample Er2 exhibited the highest J_c value of 5.5×10^4 A cm^{-2} compared to that of undoped sample Er1 under self-field (4.0×10^4 A cm^{-2}), and the current-carrying capability of Er3 (4.1×10^4 A cm^{-2}) was also better than that of Er1. In order to observe more intuitively the effect of Er₂O₃
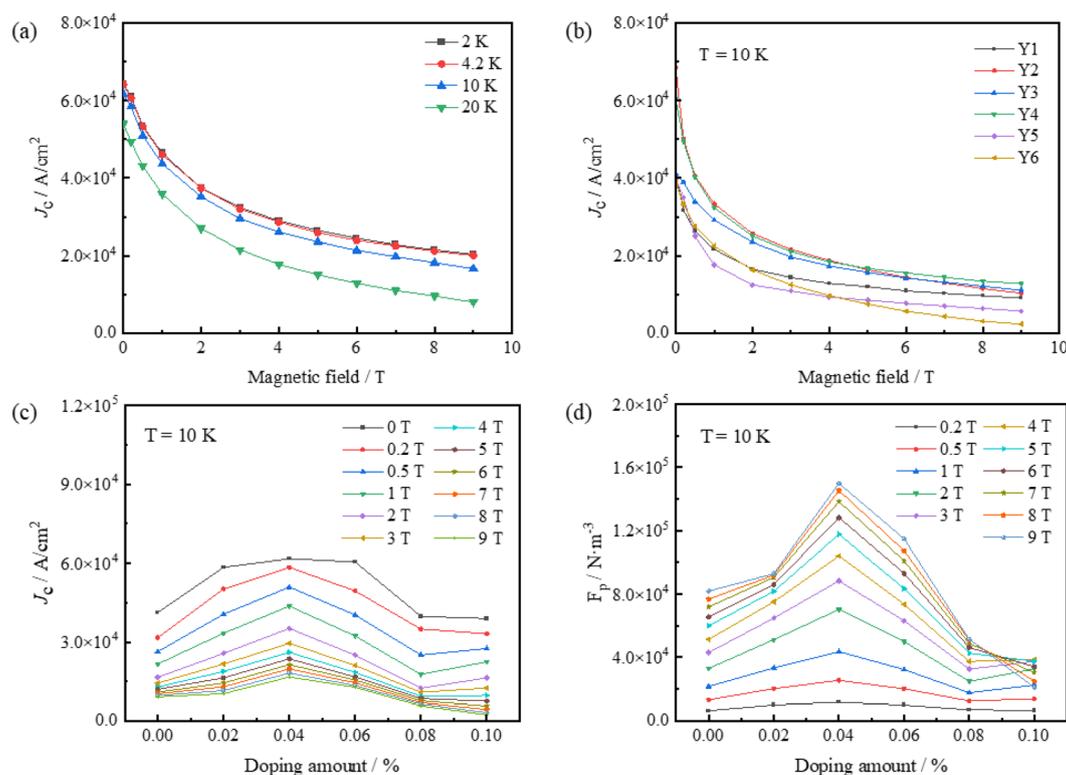

Fig. 8 (a) J_c of sample Y3 at different magnetic fields; (b) variation of J_c with magnetic field for Y group samples at 10 K; (c) variation of J_c with doping level for Y group samples at 10 K; (d) F_p versus doping level at different magnetic fields for Y group samples at 10 K.

phase doping on J_c of the Bi2212–Er-group samples, the variation of J_c with magnetic field for the Er group sample at 10 K was given in Fig. 7(b). The doping of Er_2O_3 phase significantly increased J_c of the Bi2212 superconducting films and reached the maximum value at 0.04 doping level, reaching 5.5×10^4 A cm^{-2} at 4.2 K self-field and 3.2×10^4 A cm^{-2} at 1 T vertical external field. And Er3 also showed good current-carrying capability. However, the J_c values of the samples decreased with further doping, which was attributed to the creation of excessive second-phase defects in the samples that destroyed the superconducting region and the pinning center density exceeded the coherence length of the Bi2212 films resulting in a lower J_c. To further investigate the effect of the Er_2O_3 doping density on the film properties, we calculated the macroscopic pinning force $F_p = J_c \times M$ of the samples, which is the main means to assess the flux pinning performance of superconductors. Fig. 7(d) showed the F_p for the Bi2212 films of the Er group. Sample Er2 exhibited the largest pinning force in different magnetic fields F_p. Therefore, the best pinning effect can be obtained for Er2. At this point the doping of the second phase Er_2O_3 had a more significant effect on the pinned Bi2212 superconducting film.

The effect of Y_2O_3 on the J_c of Bi2212 superconducting films was shown in Fig. 8. It can be seen from the figures that the variation pattern of J_c for all samples was consistent with that of the Er group samples. Also, it can be seen that sample Y3 exhibited the highest J_c value of 6.2×10^4 A cm^{-2} compared to that of undoped sample Y1 at self-field (4.1×10^4 A cm^{-2}), and the current-carrying capacity of Y2 and Y4 (5.8×10^4 A cm^{-2} and 6.0×10^4 A cm^{-2}) was also better than that of Y1. The variation of J_c with magnetic field for group Y samples at 10 K was also given in Fig. 8(b). The doping of the Y_2O_3 phase significantly increased the critical current density of the Bi2212 superconducting films and reached a maximum at a doping level of 0.08, reaching a critical current density of 6.2×10^4 A cm^{-2} at 10 K for the self-field and 4.3×10^4 A cm^{-2} at 1 T for the vertical external field. However, the J_c values of the samples decreased with further increase in doping. Sample Y3 exhibited the maximum pinning force F_p in different magnetic fields. Therefore, the best pinning effect for Y3 can be obtained. At this point, the doping amount of the second phase Y_2O_3 had a more significant effect on the nailing of Bi2212 superconducting films. The comparison of critical current densities J_c of different

oxide doping was listed in Table 3. The comparison showed that the doping of RE_2O_3 was also an effective method to improve the critical current density.

Conclusion

In this work, (00l) epitaxially grown Bi2212–xRE$_2O_3$ (RE = Er/Y) superconducting films were prepared by sol–gel method. The superconducting transition of the RE_2O_3-doped Bi2212 superconducting film did not change significantly with increasing doping amount, and ΔT_c increased monotonically, indicating that the RE_2O_3 phase was stacked at the grain boundaries and did not affect the lattice structure of Bi2212. The superconducting film of Er2 showed the best current-carrying capability with J_c of 5.5×10^4 A cm^{-2} at 4.2 K self-field and 3.2×10^4 A cm^{-2} at 1 T vertical external field. Y3 exhibited the best current-carrying capability with J_c of 6.2×10^4 A cm^{-2} at 10 K for the self-field and 4.3×10^4 A cm^{-2} at 1 T vertical external field. The present results provide an effective method for improving the flux pinning of Bi2212 films. And the practical application is of great importance.

Author contributions

Bowen Zhang: conceptualization, methodology, investigation, writing – original draft. Yang Qi: conceptualization, writing – review & editing.

Conflicts of interest

There are no conflicts to declare.

Acknowledgements

References

1   N. H. Mohammed, A. I. Abou-Aly, I. H. Ibrahim, *et al.*, Mechanical properties of (Cu 0.5Tl 0.5)-1223 added by nano-SnO_2, *J. Alloys Compd.*, 2009, **486**(1–2), 733–737.

2   G. Yildirim, S. Bal, E. Yucel, *et al.*, Effect of Mn Addition on Structural and Superconducting Properties of (Bi, Pb)-2223 Superconducting Ceramics, *J. Supercond. Novel Magn.*, 2012, **25**, 381–390.

3   D. Yazc, B. Zelik and M. E. Yaknc, Improvement of High T_c Phase Formation in BPSCCO Superconductor by Adding Vanadium and Substituting Titanium, *J. Low Temp. Phys.*, 2011, **163**(5–6), 370–379.

4   K. Kocaba, S. Sakiroglu, M. Ciftcioglu, *et al.*, The Effect of Zn Substitution of Ca in BiPbSrCaCuO Superconductors

Table 3   Comparison of critical current densities J_c of different oxide doping

Materials	Oxide doping	J_c (A cm^{-2}, maximum value)	Ref.
Bi2212	Er_2O_3	6.1×10^4 (4.2 K)	This work
Bi2212	Er_2O_3	5.9×10^4 (10 K)	This work
Bi2212	Y_2O_3	6.4×10^4 (4.2 K)	This work
Bi2212	Y_2O_3	6.2×10^4 (10 K)	This work
Bi2212	NiO	5.1×10^4 (10 K)	44
Bi2212	NiO	3.2×10^4 (40 K)	44
Bi2212	Al_2O_3	1.7×10^2 (77 K)	45
Bi2212	MgO	1.5×10^4 (77 K)	46
Bi2212	Pb_2O_3	6.8×10^3 (4.2 K)	47

Sintered at 830°C, *J. Supercond. Novel Magn.*, 2009, **22**(8), 749–754.

5 M. Roumié, S. Marhaba, R. Awad, *et al.*, Effect of Fe_2O_3 Nano-Oxide Addition on the Superconducting Properties of the (Bi,Pb)-2223 Phase, *J. Supercond. Novel Magn.*, 2014, **27**, 143–153.

6 H. Sözeri, N. Ghazanfari, H. Özkan, *et al.*, Enhancement in the high-T_c phase of BSCCO superconductors by Nb addition, *Supercond. Sci. Technol.*, 2007, **20**, 522–528.

7 I. Karaca, O. Uzun, U. KöLemen, *et al.*, Effects of ZnO addition on mechanical properties of $Bi_{1.84}Pb_{0.34}Sr_{1.91}Ca_{2.03}Cu_{3.06}O_{10}$ prepared by a wet technique, *J. Alloys Compd.*, 2009, **476**(1–2), 486–491.

8 S. Safran, A. Kılıç and O. Ozturk, Effect of re-pelletization on structural, mechanical and superconducting properties of BSCCO superconductors, *J. Mater. Sci.: Mater. Electron.*, 2016, **26**, 3215–3219.

9 G. Yildirim, S. Bal, E. Yucel, *et al.*, Effect of Mn Addition on Structural and Superconducting Properties of (Bi, Pb)-2223 Superconducting Ceramics, *J. Supercond. Novel Magn.*, 2011, **25**, 381–390.

10 O. Bilgili, Structural and Electrical Properties of Nanosized Sm_2O_3 Doped $Bi_{1.6}Pb_{0.4}Sr_2Ca_2Cu_3O_y$ Superconductors, *J. Low Temp. Phys.*, 2021, **204**, 223–234.

11 O. Bilgili and K. Kocabas, Effect of Nb addition on magnetic, structural and superconducting properties of (Bi, Pb)-2223 superconductors, *J. Mater. Sci.: Mater. Electron.*, 2014, **25**, 2889–2897.

12 J. M. Tarascon, P. Barboux, G. W. Hull, *et al.*, Bismuth cuprate high-Tc superconductors using cationic substitution, *Phys. Rev. B: Condens. Matter Mater. Phys.*, 1989, **39**(7), 4316–4326.

13 Y. Gao, P. Pernambuco-Wise, J. E. Crow, *et al.*, Superconducting and magnetic phase boundaries in $Bi_2Sr_2Ca_{1-x}M_xCu_2O_8$, with M=Y, Gd, and Pr, *Phys. Rev. B: Condens. Matter Mater. Phys.*, 1992, **45**, 7436–7443.

14 X. F. Sun, X. Zhao, L. Wang, *et al.*, Growth of superconducting $Bi_2Sr_2Ca(Cu_{1-x}Mn_x)_2O_y$ single crystals, *Phys. C*, 1999, **324**(3–4), 193–197.

15 V. P. Awana, L. P. Menon and S. K. Malik, Effect of substituting Ce at the Ca site on the high-temperature superconductor $Bi_2Sr_2CaCu_2O_{8+\delta}$, *Phys. Rev. B: Condens. Matter Mater. Phys.*, 1996, **53**(5), 2245–2248.

16 Q. X. Jia, B. Maiorov, H. Wang, *et al.*, Comparative study of $REBa_2Cu_3O_7$ films for coated conductors, *IEEE Trans. Appl. Supercond.*, 2005, **15**(2), 2723–2726.

17 J. L. Macmanus-Driscoll, J. A. Alonso, P. C. Wang, *et al.*, Studies of structural disorder in $ReBa_2Cu_3O_{7-x}$ thin films (Re=rare earth) as a function of rare-earth ionic radius and film deposition conditions, *Phys. C*, 1994, **232**(3–4), 288–308.

18 J. G. Lin, C. Y. Huang, Y. Y. Xue, *et al.*, Origin of the R-ion effect on T_c in $RBa_2Cu_3O_7$, *Phys. Rev. B: Condens. Matter Mater. Phys.*, 1995, **51**, 12900–12903.

19 M. Varela, D. Arias, Z. Sefrioui, *et al.*, Direct correlation between T_c and CuO_2 bilayer spacing in $YBa_2Cu_3O_{7-x}$, *Phys. Rev. B: Condens. Matter Mater. Phys.*, 2002, **66**(13), 134517.

20 A. Öztürk, I. Düzgün, Z. Sefrioui, *et al.*, The effect of partial Lu doping on magnetic behaviour of YBCO (123) superconductors, *J. Alloys Compd.*, 2010, **495**(1), 104–107.

21 J. M. Li, Extracting Superconducting Single-Crystal Nb Mesowires Out of $NbSe_2$ by a Crystal-Lattice Collapse Method, *Nano Lett.*, 2008, **8**, 1382–1385.

22 J. M. Li, X. L. Zeng, A. D. Mo, *et al.*, Fabrication of cuprate superconducting $La_{1.85}Sr_{0.15}CuO_4$ nanofibers by electrospinning and subsequent calcination in oxygen, *CrystEngComm*, 2011, **13**, 6964–6967.

23 J. M. Li and J. Fang, Anthracene-assisted inverse transport growth and superconductivity at 3.3 K in unsupported ultrathin {110} Nb and {0001} $NbSe_2$ nanoplates, *J. Mater. Chem. C*, 2017, **5**, 9545–9551.

24 J. L. Macmanus-Driscoll, S. R. Foltyn, Q. X. Jia, *et al.*, Strongly Enhanced Current Densities in Superconducting Coated Conductors of $YBa_2Cu_3O_{7-x}+BaZrO_3$, *Nat. Mater.*, 2004, **3**, 439–443.

25 Y. Yamada, K. Takahashi, H. Kobayashi, *et al.*, Epitaxial Nanostructure and Defects Effective for Pinning in Y(RE) $Ba_2Cu_3O_{7-x}$ Coated Conductors, *Appl. Phys. Lett.*, 2005, **87**(13), 132502.

26 J. Zhang, H. Y. Wu, G. Z. Zhao, *et al.*, Progress in the Study of Vortex Pinning Centers in High-Temperature Superconducting Films, *Nanomaterials*, 2022, **12**, 4000.

27 J. Zhang, H. Y. Wu, G. Z. Zhao, *et al.*, A Review on Strain Study of Cuprate Superconductors, *Nanomaterials*, 2022, **12**, 3340.

28 B. W. Zhang, Q. Guo, B. S. Dai, *et al.*, Dependence of the structure of Bi-2212 superconducting thin film prepared by sol-gel method on different complexing agents, *Ceram. Int.*, 2022, **48**, 23740–23747.

29 B. W. Zhang, Q. Guo, B. S. Dai, *et al.*, Quality optimization of Bi2212 films prepared by aqueous solvent sol-gel method with nonionic surfactants, *Ceram. Int.*, 2022, **48**, 36845–36852.

30 X. M. Lu, T. L. Wang, Y. M. Zhang, *et al.*, An enhancement in structural and superconducting properties of Bi2212 epitaxial thin films grown by the Pechini sol–gel method, *J. Appl. Crystallogr.*, 2013, **46**, 379–386.

31 T. L. Wang, X. M. Zhao and H. Z. Yang, On the roles of HEC in Pechini sol-gel method: Enhancement of stability, wettability of the sol and surface roughness of Bi2212 film, *Ceram. Int.*, 2018, **44**, 12144–12148.

32 L. Ranno, D. Martínez-García, J. Perrière, *et al.*, Phase Intergrowth in $Bi_2Sr_2Ca_{n-1}Cu_nO_y$ Thin Films, *Phys. Rev. B: Condens. Matter Mater. Phys.*, 1993, **48**, 13945–13948.

33 H. Ota, K. Sakai, Z. Mori, *et al.*, Formation of Phase Intergrowth in the Syntheses of Bi-Superconducting Thin Films, *Appl. Phys. Lett.*, 1997, **70**, 1471–1473.

34 A. L. Patterson, The Scherrer Formula for X-Ray Particle Size Determination, *Phys. Rev.*, 1939, **56**, 978–982.

35 M. Alzaid, N. M. A. Hadia, M. El-Hagary, *et al.*, Microstructural, optical, and electrical characteristics of Cu-doped CdTe nanocrystalline films for designing absorber layer in solar cell applications, *J. Mater. Sci.: Mater. Electron.*, 2021, **32**, 15095–15107.

36 M. Dehimi, T. Touam, A. Chelouche, *et al.*, Effects of Low Ag Doping on Physical and Optical Waveguide Properties of Highly Oriented Sol-Gel ZnO Thin Films, *Adv. Condens. Matter Phys.*, 2015, **2015**, 1–10.

37 Y. Iye, I. Oguro, T. Tamegai, *et al.*, Anisotropy of $Bi_2Sr_2CaCu_2O_{8+y}$ revisited, *Phys. C*, 1992, **199**, 154–160, DOI: 10.1016/0921-4534(92)90554-P.

38 S. Yamini, M. Gunaseelan, G. A. Kumar, *et al.*, Tailoring the upconversion emission and magnetic properties of $NaGdF_4$:Yb, Er by Mg^{2+} or Fe^{3+} doping and optical trapping of individual magnetic nanoparticle at NIR 980 nm, *Ceram. Int.*, 2022, **16**, 48.

39 M. Subhajit, D. Tanushri, D. Sagnik, *et al.*, Y and Al co-doped ZnO-nanopowder based ultrasensitive trace ethanol sensor: a potential breath analyzer for fatty liver disease and drunken driving detection, *Sens. Actuators, B*, 2022, **372**, 132611.

40 C. Cai, B. Holzapfel, J. Hänisch, *et al.*, Direct evidence for tailorable flux-pinning force and its anisotropy in$RBa_2Cu_3O_{7-\delta}$ multilayers, *Phys. Rev. B: Condens. Matter Mater. Phys.*, 2004, **70**, 212501, DOI: 10.1103/PhysRevB.70.212501.

41 H. E. Ouaddi, A. Tirbiyine, A. Taoufik, *et al.*, Magnetization Measurements in the 80 K Transformation for Deuterated Organic Superconductor κ-(BEDT-TTF)$_2$Cu[N(CN)$_2$]Br, *Mod. Phys. Lett. B*, 2013, **27**, 1350037.

42 J. R. Cooper, J. W. Loram and J. D. Johnson, 3D *XY* Scaling of the Irreversibility Line of $YBa_2Cu_3O_7$ Crystals, *Phys. Rev. Lett.*, 1997, **79**, 1730–1733.

43 M. Li, Y. Zhang, Y. Li, *et al.*, Granular Superconductivity in Polycrystalline $Bi_2Sr_2CaCu_2O_{8+\delta}$ by Homovalent La Substitution on Bi Sites, *J. Non-Cryst. Solids*, 2010, **356**(50), 2831–2835.

44 X. M. Zhao, W. B. Liu, T. L. Wang, *et al.*, Growth of $Bi_2Sr_2CaCu_2O_{8+\delta}$ thin films with enhanced superconducting properties by incorporating NiO nanoparticles, *Colloids Surf., A*, 2021, **627**, 127121.

45 M. Annabi, A. M'chirgui, F. B. Azzouz, *et al.*, Addition of nanometer Al2O3 during the final processing of (Bi, Pb)-2223 superconductors, *Phys. C*, 2004, **405**, 25–33.

46 I. E. Agranovski, A. Y. Ilyushechkin, I. S. Altmana, *et al.*, Methods of introduction of MgO nanoparticles into Bi-2212/Ag tapes, *Phys. C*, 2006, **434**, 115–120.

47 R. Funahashi, I. Matsubara, K. Ueno, *et al.*, Isotropic pinning in heavily Pb-doped Bi-2212/Ag tapes, *Phys. C*, 2015, **315**, 247–253.